14 Dense Granular Avalanches: Mathematical Description and Experimental Validation

Y.-C. Tai[1], K. Hutter[1], and J.M.N.T. Gray[2]

[1] Institute of Mechanics, Darmstadt University of Technology
Hochschulstr. 1, 64289 Darmstadt, Germany
[2] Department of Mathematics, University of Manchester, Manchester M13 9PL, UK

14.1 Introduction

Snow avalanches, landslides, rock falls and debris flows are extremely dangerous and destructive natural phenomena. The frequency of occurrence and amplitudes of these disastrous events appear to have increased in recent years perhaps due to recent climate warming. The events endanger the personal property and infra-structure in mountainous regions. For example, from the winters 1940/41 to 1987/88 more than 7000 snow avalanches occurred in Switzerland with damaged property leading to a total of 1269 deaths. In February 1999, 36 people were buried by a single avalanche in Galtür, Austria. In August 1996, a very large debris flow in middle Taiwan resulted in 51 deaths, 22 lost and an approximate property damage of more than 19 billion NT dollars (ca. 600 million US dollars) [18]. In Europe, a suddenly released debris flow in North Italy in August 1998 buried 5 German tourists on the Superhighway "Brenner–Autobahn". The topic has gained so much significance that in 1990 the United Nations declared the *International Decade for Natural Disasters Reduction (IDNDR)*; Germany has its own *Deutsches IDNDR–Komitee für Katastrophenvorbeugung e.V.* Special conferences are devoted to the theme, e.g. , the CALAR conference on Avalanches, Landslides, Rock Falls and Debris Flows (Vienna, January 2000), *INTERPRAEVENT*, annual conferences on the *protection of habitants from floods, debris flows and avalanches*, special conferences on debris flow hazard mitigation and those exclusively on *Avalanches*.

With increasing population and with the popularization of the tourism in the mountainous regions the damage equally increases, occasionally leading to excessive devastation. Reliable methods for the prevention or reduction of the effects of such disasters consist, on the one hand, in predicting the disaster itself and, on the other hand, in the determination of the likely paths of the flows, the maximum run-out distances as well as the protection against such destructive flows. They are of considerable interest to civil and environmental engineers and civil servants of municipalities responsible for the planning and development in populated mountainous regions. The Savage–Hutter theory [19,20] and its three-dimensional extension [4,15] for the gravity-driven, free-surface flow of granular material has proved to model such flows adequately and is now established as one of the leading models for this purpose. We will show in these lecture notes, how these model equations can be constructively used to describe these flows.

N.J. Balmforth and A. Provenzale (Eds.): LNP 582, pp. 339–366, 2001.

A successful verification of an avalanche model by laboratory experiments is a necessary requirement for it to have a chance also to be adequate in realistic situations. This second proof still needs to be completed by applying it to a real avalanche event. For the time being, we are confident on the basis that our model extends a well established model of Voellmy [26] to account for the important geometric deformations of an avalanche along its track. Entrainment of material along the avalanche track can be incorporated, and is a very significant process in real avalanches, but it is not yet incorporated in our model, because no experimental method has so far been found by which an entrainment model could be verified in the laboratory. Entrainment to and deposition from a moving granular mass are however very significant in realistic flows and constitute the "last" unsolved item in the mathematical model to be presented below.

Reviews on the subject are e.g. given in [8,9]. A further article on avalanches – mostly from the practical side – is given by Ancey (Chap. 13).

14.2 The Granular Avalanche Model of Savage & Hutter [1]

The Savage–Hutter theory [19] is a continuum theory to describe the two-dimensional motion of a finite mass avalanche over a rough inclined slope[2]. The dry cohesionless granular material is assumed to be incompressible with constant density ρ_0 throughout the entire body. During flow the body behaves as a Mohr–Coulomb plastic material at yield, which slides over a rigid basal topography. Scaling analysis isolates the physically significant terms in the governing equations and identifies those terms that can be neglected. Finally, depth integration reduces the theory by one spatial dimension.

A simple curvilinear coordinate system was introduced by Savage & Hutter [20] to enable the avalanche motion to be modelled from initiation on a steep slope to run-out on a rough curved bed. The coordinates are defined and aligned with the curved rigid basal topography, so that the local inclination angle ζ varies as a function of the downslope coordinate x.

The Savage–Hutter theory has been extended to three-dimensions by Hutter et al. [15], Greve et al. [6], Gray et al. [4], and Wieland et al. [27] for the case of

[1] This section is taken from [24].

[2] All avalanche models known to us and used in practice are essentially based on Voellmy's [26] original model, which may be interpreted as a rigid mass or hydraulic model (depending on view point). In these models, the physics is incorporated in the parameterization of the resistive forces comprising of a Coulomb and a viscous type contribution. The modern trend is to use the basic balance laws of physics and to account for the internal physics as well as the variation of the basal topography, just as attempted in the Savage–Hutter model in a very simple form. There have been attempts to model avalanches by molecular dynamics procedures, and these are successful when the number of particles or grains is small, i.e. a few hundred or thousand, as e.g. in rock falls. Possible farther reaching conceptual formulations of both the continuum and molecular dynamics concepts are given in Chap. 4 and the literature cited there.

unconfined three-dimensional flow. Hutter et al. [15] derived the leading order equations for the motion of unconfined flow on an inclined plane with constant inclination angle. Greve et al. [6] introduced a quasi one-dimensional curvilinear system to model unconfined flow on a simple chute without lateral curvature, whilst Gray et al. [4] generalized this theory to allow the flow over complex three-dimensional topography. The final three-dimensional theory is able to predict the flow over realistic topography and provide information about the maximum run-out distance in site specific applications.

In this section a brief introduction to the Savage–Hutter theory and its three-dimensional extension over realistic topography is given. Different from the procedure of the original derivation in [19], the governing equations are integrated through the depth before the procedure of scaling analysis. In accordance with the conservation laws of mass and linear momentum the governing equations are derived in conservative form as described in [4], which will be used to model granular shocks that have been observed in laboratory experiments, as they are in conservative form and therefore allow discontinuities in the physical variables to be considered.

14.2.1 Governing Equations in Conservative Form

The avalanche is treated as a material with constant density[3] ρ_0 throughout the entire avalanche body, the local differential forms of the mass and momentum conservation laws are therefore

$$\operatorname{div} \boldsymbol{v} = 0 \,, \tag{14.1a}$$

$$\rho_0 \Big\{ \frac{\partial \boldsymbol{v}}{\partial t} + \operatorname{div} (\boldsymbol{v} \otimes \boldsymbol{v}) \Big\} = -\operatorname{div} \boldsymbol{p} + \rho_0 \, \boldsymbol{g} \,, \tag{14.1b}$$

where $\boldsymbol{v}$ is the velocity, $\otimes$ the dyadic product, $\boldsymbol{p}$ the pressure tensor and $\boldsymbol{g}$ the gravitational acceleration.

Following [19], the body is assumed to have Mohr–Coulomb constitutive properties. This implies that yield occurs when the internal shear stress S and the normal pressure N are related by

$$|S| = N \tan\phi \,, \tag{14.2}$$

where ϕ is the so-called internal friction angle.

The body is subject to kinematic and traction boundary conditions at the free surface $F^s(\boldsymbol{x}, t) = 0$ and at the base $F^b(\boldsymbol{x}, t) = 0$ of the avalanche. The kinematic boundary conditions are

$$\frac{\partial F^s}{\partial t} + \boldsymbol{v}^s \cdot \operatorname{grad} F^s = 0 \,, \tag{14.3}$$

$$\frac{\partial F^b}{\partial t} + \boldsymbol{v}^b \cdot \operatorname{grad} F^b = 0 \,, \tag{14.4}$$

[3] Possible sizable volume changes occur at the instants of avalanche inception and settling, but not so much during motion, see [12]. This is the reason, why a density preserving model delivers good results.

where the superscripts s and b indicate the variable evaluated at the free surface and at the base, respectively. Note that for a rigid basal topography, $F^b(\boldsymbol{x}) = 0$, the kinematic boundary condition reduces to $\boldsymbol{v}^b \cdot \operatorname{grad} F^b = 0$, which implies that the avalanche slides on the basal surface without inflow or outflow, i.e. an impenetrable base.

The kinematic free surface of the avalanche is assumed to be traction free, and at the base a sliding Coulomb dry friction law[4] is applied. That is,

$$\boldsymbol{p}^s \boldsymbol{n}^s = \boldsymbol{0} \,, \tag{14.5}$$

$$\boldsymbol{p}^b \boldsymbol{n}^b - \left(\boldsymbol{n}^b \cdot \boldsymbol{p}^b \boldsymbol{n}^b\right) \boldsymbol{n}^b = (\boldsymbol{v}^b / |\boldsymbol{v}^b|) N^b \tan\delta \,, \tag{14.6}$$

where $(\boldsymbol{pn})_i = p_{ij} n_j$, $N^b = \boldsymbol{n}^b \cdot \boldsymbol{p}^b \boldsymbol{n}^b$ indicates the normal pressure at the base of the avalanche, δ is the basal angle of friction, $\boldsymbol{n}^s$ and $\boldsymbol{n}^b$ are outward pointing normal vectors at the free surface and base, respectively,

$$\boldsymbol{n}^s = \frac{\nabla F^s}{|\nabla F^s|} \,, \qquad \boldsymbol{n}^b = \frac{\nabla F^b}{|\nabla F^b|} \,. \tag{14.7}$$

14.2.2 Curvilinear Coordinate System

An orthogonal curvilinear coordinate system, $Oxyz$, is defined by a reference surface [4], which is illustrated in Fig. 14.1a. The x axis is oriented in the downslope direction, the y axis lies in the cross slope direction to the reference surface and the z axis is normal to it. The downslope inclination angle of the reference surface ζ, to the horizontal, changes as a function of the downslope coordinate x, and there is no lateral variation in the y direction. The complex shallow basal topography is defined by its elevation $z = z^b(x, y)$ above the reference surface, as illustrated in Fig. 14.1b. The region above the reference surface $z = 0$ can be described by the coordinates xyz that is based on the metric with the squared arc length

$$\mathrm{d}s^2 = (1 - \kappa z)^2 \mathrm{d}x^2 + \mathrm{d}y^2 + \mathrm{d}z^2 \,, \tag{14.8}$$

where $\kappa = -\partial\zeta/\partial x$ is the curvature of the reference surface. The metric defines each point in a domain of the three-dimensional space uniquely as long as the z-coordinate is locally smaller than $1/\kappa$. In the ensuing analysis this will automatically be assumed.

In this curvilinear coordinate system the divergence of the velocity $\boldsymbol{v}$ in (14.1a) is

$$\nabla \cdot \boldsymbol{v} = \frac{\partial}{\partial x}(\psi u) + \frac{\partial v}{\partial y} + \frac{\partial w}{\partial z} - \psi^2 \kappa' z u - \psi \kappa w \,, \tag{14.9}$$

where $\psi = 1/(1 - \kappa z)$ and u, v, w are the physical velocity components in the x, y and z directions, respectively. $\kappa' = \partial\kappa/\partial x$ is the derivative of the curvature

[4] An elementary account on the Coulomb law is given in Chap. 4.

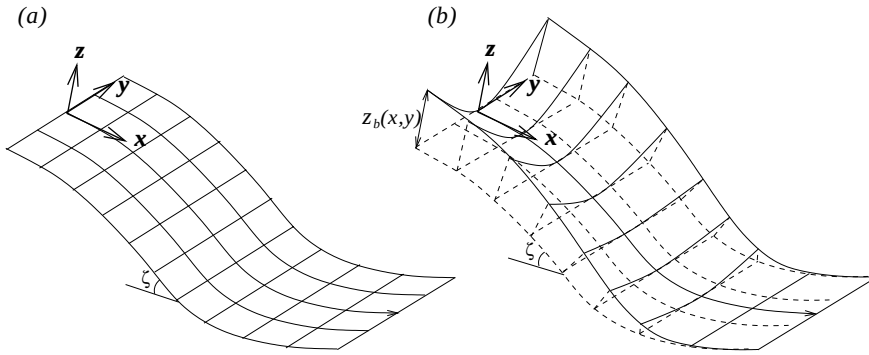

Fig. 14.1. (**a**) The curvilinear reference surface which defines the curvilinear coordinate system $Oxyz$, where the downslope inclination angle of the reference surface ζ, to the horizontal, changes as a function of the downslope coordinate x. (**b**) The shallow basal topography is defined by its height $z = z^b(x, y)$ above the curvilinear reference surface

with respect to the downslope coordinate x. In the curvilinear coordinate system the divergence of a second order tensor $\boldsymbol{T}$ [6,4] is expressed by

$$\begin{aligned}\nabla\cdot\boldsymbol{T} = &\left\{\frac{\partial}{\partial x}\big(\psi T_{xx}\big)+\frac{\partial T_{xy}}{\partial y}+\frac{\partial T_{xz}}{\partial z}-\psi^2\kappa' z T_{xx}-2\psi\kappa T_{xz}\right\}\boldsymbol{e}_x\\ &+\left\{\frac{\partial}{\partial x}\big(\psi T_{xy}\big)+\frac{\partial T_{yy}}{\partial y}+\frac{\partial T_{yz}}{\partial z}-\psi^2\kappa' z T_{xy}-\ \psi\kappa T_{yz}\right\}\boldsymbol{e}_y\\ &+\left\{\frac{\partial}{\partial x}\big(\psi T_{xz}\big)+\frac{\partial T_{yz}}{\partial y}+\frac{\partial T_{zz}}{\partial z}-\psi^2\kappa' z T_{xz}-\psi\kappa(T_{zz}-T_{xx})\right\}\boldsymbol{e}_z\ ,\end{aligned} \tag{14.10}$$

where $\boldsymbol{e}_x$, $\boldsymbol{e}_y$ and $\boldsymbol{e}_z$ are the unit vectors in the downslope, cross slope and normal directions, respectively. Furthermore, the gradient of a scalar field F in this curvilinear coordinate system is

$$\nabla F=\frac{1}{1-\kappa z}\frac{\partial F}{\partial x}\boldsymbol{e}_x+\frac{\partial F}{\partial y}\boldsymbol{e}_y+\frac{\partial F}{\partial z}\boldsymbol{e}_z\ . \tag{14.11}$$

Using (14.9) the mass balance equation (14.1a) becomes

$$\frac{\partial}{\partial x}(\psi u)+\frac{\partial v}{\partial y}+\frac{\partial w}{\partial z}-\psi^2\kappa' z u-\psi\kappa w=0\ . \tag{14.12}$$

By virtue of (14.9) and (14.10), the downslope, cross slope and normal components of the momentum balance equations are

$$\begin{aligned}&\rho_0\left\{\frac{\partial u}{\partial t}+\frac{\partial}{\partial x}(\psi u^2)+\frac{\partial}{\partial y}(uv)+\frac{\partial}{\partial z}(uw)-\kappa' z\psi^2u^2-2\kappa\psi uw\right\}\\ &=\rho_0 g\sin\zeta-\frac{\partial}{\partial x}\big(\psi p_{xx}\big)-\frac{\partial}{\partial y}\big(p_{xy}\big)-\frac{\partial}{\partial z}\big(p_{xz}\big)+\kappa' z\psi^2p_{xx}+2\kappa\psi p_{xz}\ ,\end{aligned} \tag{14.13}$$

$$\rho_0\left\{\frac{\partial v}{\partial t}+\frac{\partial}{\partial x}(\psi uv)+\frac{\partial}{\partial y}(v^2)+\frac{\partial}{\partial z}(vw)-\kappa' z\psi^2 uv-\kappa\psi vw\right\}$$
$$=\quad -\frac{\partial}{\partial x}\big(\psi p_{xy}\big)-\frac{\partial}{\partial y}\big(p_{yy}\big)-\frac{\partial}{\partial z}\big(p_{yz}\big)+\kappa' z\psi^2 p_{xy}+\kappa\psi p_{yz}\ , \tag{14.14}$$

$$\rho_0\left\{\frac{\partial w}{\partial t}+\frac{\partial}{\partial x}(\psi uw)+\frac{\partial}{\partial y}(vw)+\frac{\partial}{\partial z}(w^2)-\kappa' z\psi^2 uw-\kappa\psi(w^2-u^2)\right\}$$
$$=-\rho_0 g\cos\zeta-\frac{\partial}{\partial x}\big(\psi p_{xz}\big)-\frac{\partial}{\partial y}\big(p_{yz}\big)-\frac{\partial}{\partial z}\big(p_{zz}\big)+\kappa' z\psi^2 p_{xz} \tag{14.15}$$
$$+\kappa\psi(p_{zz}-p_{xx})\ ,$$

respectively, where $p_{ij},\ i,\ j=x,\ y,\ z$ are the components of the pressure tensor in this curvilinear coordinate system. The free and basal surfaces are defined by their heights above the reference surface,

$$\begin{aligned} F^s(\boldsymbol{x},t)&=z-z^s(x,y,t)=0\ ,\\ F^b(\boldsymbol{x},t)&=z^b(x,y,t)-z=0\ , \end{aligned} \tag{14.16}$$

which ensure the normals $\boldsymbol{n}^s$ and $\boldsymbol{n}^b$ point outwards from the avalanche body. The kinematic boundary conditions reduce to

$$-\frac{\partial z^s}{\partial t}-\psi^s u^s\frac{\partial z^s}{\partial x}-v^s\frac{\partial z^s}{\partial y}+w^s=0 \tag{14.17}$$

for the free surface and

$$\frac{\partial z^b}{\partial t}+\psi^b u^b\frac{\partial z^b}{\partial x}+v^b\frac{\partial z^b}{\partial y}-w^b=0 \tag{14.18}$$

for the base, where we recall that the superscripts s, b indicate the values at the free and basal surface, respectively. The traction condition on the free surface (14.5) yields

$$\begin{aligned} -p^s_{xx}\psi^s\frac{\partial z^s}{\partial x}-p^s_{xy}\frac{\partial z^s}{\partial y}+p^s_{xz}&=0\ ,\\ -p^s_{xy}\psi^s\frac{\partial z^s}{\partial x}-p^s_{yy}\frac{\partial z^s}{\partial y}+p^s_{yz}&=0\ ,\\ -p^s_{xz}\psi^s\frac{\partial z^s}{\partial x}-p^s_{yz}\frac{\partial z^s}{\partial y}+p^s_{zz}&=0\ , \end{aligned} \tag{14.19}$$

and the sliding condition at the base (14.6) becomes

$$\begin{aligned} p^b_{xx}\psi^b\frac{\partial z^b}{\partial x}+p^b_{xy}\frac{\partial z^b}{\partial y}-p^b_{xz}&=\Big(\psi^b\frac{\partial z^b}{\partial x}+|\nabla F^b|\frac{u^b}{|\boldsymbol{v}^b|}\tan\delta\Big)N^b\ ,\\ p^b_{xy}\psi^b\frac{\partial z^b}{\partial x}+p^b_{yy}\frac{\partial z^b}{\partial y}-p^b_{yz}&=\Big(\quad\frac{\partial z^b}{\partial y}+|\nabla F^b|\frac{v^b}{|\boldsymbol{v}^b|}\tan\delta\Big)N^b\ ,\\ p^b_{xz}\psi^b\frac{\partial z^b}{\partial x}+p^b_{yz}\frac{\partial z^b}{\partial y}-p^b_{zz}&=-N^b\ , \end{aligned} \tag{14.20}$$

where $\psi^b = 1/(1-\kappa z^b)$. The Coulomb dry friction shear traction is related by the normal basal pressure N^b and the bed friction angle δ. Applying the definitions of the normal basal pressure $N^b = \boldsymbol{n}^b \cdot \boldsymbol{p}^b \boldsymbol{n}^b$ and the basal normal vector (14.7) yields

$$N^b = \frac{1}{|\nabla F^b|^2}\left\{(\psi^b)^2\left(\frac{\partial z^b}{\partial x}\right)^2 p^b_{xx} + 2\psi^b\left(\frac{\partial z^b}{\partial x}\right)\left(\frac{\partial z^b}{\partial y}\right)p^b_{xy} \right. \\ \left. -2\psi^b\left(\frac{\partial z^b}{\partial x}\right)p^b_{xz} + \left(\frac{\partial z^b}{\partial y}\right)^2 p^b_{yy} - 2\left(\frac{\partial z^b}{\partial y}\right)p^b_{yz} + p^b_{zz}\right\} . \tag{14.21}$$

14.2.3 Depth Integration

The mass and momentum balance equations are integrated through the avalanche depth to simplify the problem. The avalanche thickness (depth) is the difference between the height of the free surface z^s and the height of the basal topography z^b

$$h = z^s - z^b , \tag{14.22}$$

and is measured normal to the reference surface. The depth integrated mean value is denoted by $\langle\cdot\rangle$ and defined by

$$\langle f\rangle = \frac{1}{h}\int_{z^b}^{z^s} f \,\mathrm{d}z \tag{14.23}$$

for any field quantity f.

Using Leibniz's rule and integrating the mass balance equation (14.9) through the avalanche depth subject to the kinematic boundary conditions at the free (14.17) and basal (14.18) surfaces in the curvilinear coordinate system, it follows that

$$\frac{\partial h}{\partial t} + \frac{\partial}{\partial x}(h\langle\psi u\rangle) + \frac{\partial}{\partial y}(h\langle v\rangle) - \kappa' h\langle\psi^2 z u\rangle - \kappa h\langle\psi w\rangle = 0 . \tag{14.24}$$

Similarly, integrating the linear momentum balance equations, (14.13), (14.14) and (14.15), through the avalanche depth and applying the kinematic as well as traction boundary conditions at both the free surface (14.17), (14.19) and the basal surface (14.18), (14.20), the depth integrated downslope, cross slope and normal components of the momentum balance are

$$\rho_0\Big\{\frac{\partial}{\partial t}(h\langle u\rangle) + \frac{\partial}{\partial x}(h\langle\psi u^2\rangle) + \frac{\partial}{\partial y}(h\langle uv\rangle) - \kappa' h\langle\psi^2 z u^2\rangle - 2\kappa h\langle\psi uw\rangle\Big\} \\ = \rho_0 g h\sin\zeta - \frac{\partial}{\partial x}\big(h\langle\psi p_{xx}\rangle\big) - \frac{\partial}{\partial y}(h\langle p_{xy}\rangle) \\ - \left(\psi^b\frac{\partial z^b}{\partial x} + |\nabla F^b|\frac{u^b}{|\boldsymbol{v}^b|}\tan\delta\right)N^b + \kappa' h\langle\psi^2 z p_{xx}\rangle + 2\kappa h\langle\psi p_{xz}\rangle , \tag{14.25}$$

$$\rho_0\Big\{\frac{\partial}{\partial t}(h\langle v\rangle)+\frac{\partial}{\partial x}(h\langle\psi uv\rangle)+\frac{\partial}{\partial y}(h\langle v^2\rangle)-\kappa' h\langle\psi^2 zuv\rangle-\kappa h\langle\psi vw\rangle\Big\}$$
$$=\quad -\frac{\partial}{\partial x}\big(h\langle\psi p_{xy}\rangle\big)-\frac{\partial}{\partial y}(h\langle p_{yy}\rangle)$$
$$-\left(\frac{\partial z^b}{\partial y}+|\nabla F^b|\frac{v^b}{|\boldsymbol{v}^b|}\tan\delta\right)N^b+\kappa' h\langle\psi^2 zp_{xy}\rangle+\kappa h\langle\psi p_{yz}\rangle\ , \tag{14.26}$$

$$\rho_0\Big\{\frac{\partial}{\partial t}(h\langle w\rangle)+\frac{\partial}{\partial x}(h\langle\psi uw\rangle)+\frac{\partial}{\partial y}(h\langle vw\rangle)-\kappa' h\langle\psi^2 zuw\rangle-\kappa h\langle\psi(w^2-u^2)\rangle\Big\}$$
$$=-\rho_0 gh\cos\zeta-\frac{\partial}{\partial x}\big(h\langle\psi p_{xz}\rangle\big)-\frac{\partial}{\partial y}(h\langle p_{yz}\rangle)$$
$$+N^b+\kappa' h\langle\psi^2 zp_{xz}\rangle+\kappa h\langle\psi(p_{zz}-p_{xx})\rangle\ , \tag{14.27}$$

respectively. For details of the derivation see [4].

14.2.4 Non-Dimensionalization and Ordering

Three length scales are introduced to isolate the physically significant terms in the governing equations, a longitudinal length scale, L, a depth scale, H, and a scale for the basal curvature in the downslope direction, $1/R$. Following [19], [6] and [4], the physical variables are non-dimensionalized using the scalings

$$\begin{aligned}
\big(x,\,y,\,z\big)_{\rm dim}&=L\big(x,\,y,\,\varepsilon z\big)_{\rm non-dim}\ ,\\
\big(u,\,v,\,w\big)_{\rm dim}&=\sqrt{gL}\big(u,\,v,\,\varepsilon\,w\big)_{\rm non-dim}\ ,\\
\big(p_{xx},\,p_{yy},\,p_{zz},\,N^b\big)_{\rm dim}&=\rho_0 gH\big(p_{xx},\,p_{yy},\,p_{zz},\,N^b\big)_{\rm non-dim}\ ,\\
\big(p_{xy},\,p_{xz},\,p_{yz}\big)_{\rm dim}&=\rho_0 gH\mu\big(p_{xy},\,p_{xz},\,p_{yz}\big)_{\rm non-dim}\ ,\\
(t)_{\rm dim}&=\sqrt{L/g}\,(t)_{\rm non-dim}\ ,\\
(\kappa)_{\rm dim}&=1/R\,(\kappa)_{\rm non-dim}\ ,
\end{aligned} \tag{14.28}$$

where $\varepsilon = H/L$ is the aspect ratio and μ indicates a typical magnitude of the friction coefficient, $\tan\delta_0$.

Observations of avalanches in nature and laboratory experiments suggest that they are long and thin and that the basal surfaces on which they slide often have shallow curvature. The shallowness assumption for the avalanche geometry implies that the aspect ratio of the avalanche is small,

$$\varepsilon = H/L \ll 1\ . \tag{14.29}$$

The measure of the curvature of the reference surface geometry with respect to the length of the avalanche $\lambda = L/R$ and the friction coefficient μ are assumed to be of magnitude [4]

$$\lambda=\mathcal{O}(\varepsilon^{\alpha})\ ,\quad \mu=\mathcal{O}(\varepsilon^{\beta})\ ,\quad 0<\alpha\ ,\ \ \beta<1\ . \tag{14.30}$$

Applying the scalings (14.28) and assumption (14.30), it follows that the depth integrated non-dimensional mass balance equation in curvilinear form is

$$\frac{\partial h}{\partial t} + \frac{\partial}{\partial x}(h\langle u\rangle) + \frac{\partial}{\partial y}(h\langle v\rangle) = 0 + \mathcal{O}(\varepsilon^{1+\alpha}) \,, \tag{14.31}$$

where all variables in this equation and in the remainder of this text are now non-dimensional unless stated otherwise. Using (14.28) the normal component of the momentum balance (14.15) reduces to

$$\frac{\partial p_{zz}}{\partial z} = -\cos\zeta + \mathcal{O}(\varepsilon^{\alpha}) \,, \tag{14.32}$$

which implies that p_{zz} varies linearly with respect to z to order ε^{α}. The normal basal pressure (14.21) gives $N_b = p^b_{zz} + \mathcal{O}(\varepsilon^{1+\beta})$ that the normal component of the non-dimensional depth integrated momentum balance (14.27) reduces to

$$p^b_{zz} = \lambda\kappa h\langle u^2\rangle + h\cos\zeta + \mathcal{O}(\varepsilon) \,. \tag{14.33}$$

The downslope and cross slope components are

$$\begin{aligned} &\frac{\partial}{\partial t}(h\langle u\rangle) + \frac{\partial}{\partial x}(h\langle u^2\rangle) + \frac{\partial}{\partial y}(h\langle uv\rangle) \\ &\qquad = h\sin\zeta - \varepsilon\frac{\partial}{\partial x}(h\langle p_{xx}\rangle) - \varepsilon h\cos\zeta\frac{\partial z^b}{\partial x} \\ &\qquad\qquad - \frac{u^b}{|\boldsymbol{v}^b|}h\tan\delta(\cos\zeta + \lambda\kappa\langle u^2\rangle) + \mathcal{O}(\varepsilon^{1+\gamma}) \,, \end{aligned} \tag{14.34}$$

$$\begin{aligned} &\frac{\partial}{\partial t}(h\langle v\rangle) + \frac{\partial}{\partial x}(h\langle uv\rangle) + \frac{\partial}{\partial y}(h\langle v^2\rangle) \\ &\qquad = \qquad - \varepsilon\frac{\partial}{\partial y}(h\langle p_{yy}\rangle) - \varepsilon h\cos\zeta\frac{\partial z^b}{\partial y} \\ &\qquad\qquad - \frac{v^b}{|\boldsymbol{v}^b|}h\tan\delta(\cos\zeta + \lambda\kappa\langle u^2\rangle) + \mathcal{O}(\varepsilon^{1+\gamma}) \,, \end{aligned} \tag{14.35}$$

respectively, in which $\gamma = \min(\alpha, \beta)$.

14.2.5 Earth Pressure Coefficients

In the original Savage–Hutter theory [19,20] the stress state of the avalanche is assumed to satisfy both the Coulomb sliding friction law and the internal yield criterion simultaneously at the base of the avalanche. In addition, since the motion is predominantly downslope it is assumed that the basal cross slope pressure, p^b_{yy}, is a principal stress and that it is equal to one of the other two principal stresses in the xz plane. The details of this analysis have been performed many times and are well documented in the literature, see e.g. [4,5,6,7,8,9,12,13,14,15,17,19,20], the most useful references probably being [6,17].

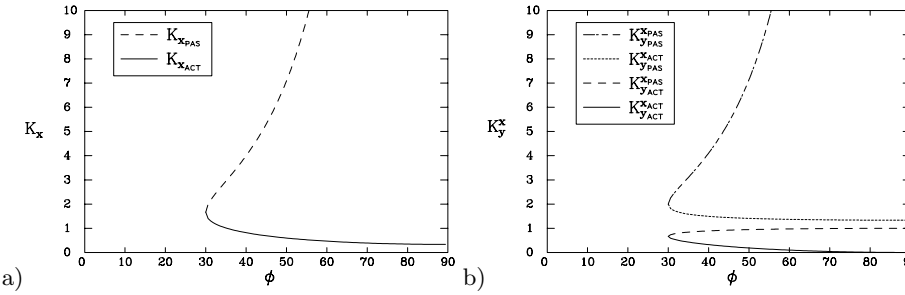

Fig. 14.2. The downslope (**a**) and cross slope (**b**) earth pressure coefficients are plotted as functions of the internal friction angle ϕ with constant bed friction angle $\delta = 30°$. The various active and passive stress states are indicated by different line styles

Under these assumptions two Mohr stress circles can be constructed that satisfy the yield criterion and the sliding law. For the basal normal pressure, p^b_{zz}, and the shear stress, $-p^b_{xz}$, the basal down slope pressure, p^b_{xx}, can therefore assume two values, one on the larger circle, $p^b_{xx} > p^b_{zz}$, and the other on the smaller circle, $p^b_{xx} < p^b_{zz}$. These downslope and normal pressures can be related by introducing the earth pressure coefficient $K^b_x = p^b_{xx}/p^b_{zz}$. Using elementary geometrical arguments K^b_x is described as a function of the internal and basal friction angles [19]

$$K^b_{x_{\mathrm{act/pass}}} = 2\left(1 \mp \sqrt{1 - \cos^2\phi/\cos^2\delta}\right)\sec^2\phi - 1\,. \tag{14.36}$$

This is real valued provided $\delta \le \phi$. Savage & Hutter [19] made the *ad hoc* definition that the *active* state was associated with divergent motion and the *passive* state was associated with convergent motion, i.e.

$$K^b_x = \begin{cases} K^b_{x_{\mathrm{act}}} & \partial u/\partial x \ge 0\,, \\ K^b_{x_{\mathrm{pass}}} & \partial u/\partial x < 0\,. \end{cases} \tag{14.37}$$

The left panel in Fig. 14.2 illustrates the values of $K^b_{x_{\mathrm{act/pass}}}$ as a function of the internal friction angle ϕ for constant basal friction angle $\delta = 30°$. When $\phi = \delta$ the active and passive earth pressure coefficients are equal, $K^b_{x_{\mathrm{act}}} = K^b_{x_{\mathrm{pass}}}$. For $\phi < \delta$ the earth pressure coefficients are not real valued.

As mentioned above, the basal cross slope pressure is equal to one of the other two principal stresses in the xz plane. Introducing the cross slope earth pressure coefficient at the base, $K^b_y = p^b_{yy}/p^b_{zz}$, Hutter et al. [13] showed that it is equal to

$$K^b_{y_{\mathrm{act/pass}}} = \frac{1}{2}\left(K^b_x + 1 \mp \sqrt{(K^b_x - 1)^2 + 4\tan^2\delta}\right)\,, \tag{14.38}$$

which is not only a function of the internal and basal friction angle but also depends on the downslope earth pressure coefficient. Since there are two principal

stresses for the Mohr stress circle determined by the stress state in the xz plane, there are four possible stress states for the cross slope pressure. As in the two-dimensional theory they are distinguished from one another by *ad hoc* definitions dependent upon whether the downslope and cross slope deformation is divergent or convergent [13],

$$K_y^b = \begin{cases} K_{y_{\rm act}}^{x_{\rm act}} & \partial u/\partial x \geq 0\ ,\ \partial v/\partial y \geq 0\ , \\ K_{y_{\rm pass}}^{x_{\rm act}} & \partial u/\partial x \geq 0\ ,\ \partial v/\partial y < 0\ , \\ K_{y_{\rm act}}^{x_{\rm pass}} & \partial u/\partial x < 0\ ,\ \partial v/\partial y \geq 0\ , \\ K_{y_{\rm pass}}^{x_{\rm pass}} & \partial u/\partial x < 0\ ,\ \partial v/\partial y < 0\ . \end{cases} \tag{14.39}$$

In the first of these inequalities the flow is extending in both the x- and y-directions, in the last it is contracting in the two directions. In the right panel of Fig. 14.2, K_y^b is illustrated as a function of the internal friction angle ϕ for constant $\delta = 30°$. Like the downslope earth pressure coefficient, K_y is real valued if and only if $\delta \leq \phi$ and $K_{y_{\rm act}}^b = K_{y_{\rm pass}}^b$ when $\delta = \phi$. In addition the earth pressure coefficients are ordered in the following way: $K_{y_{\rm act}}^{x_{\rm act}} \leq K_{y_{\rm act}}^{x_{\rm pas}} < K_{y_{\rm pas}}^{x_{\rm act}} \leq K_{y_{\rm pas}}^{x_{\rm pas}}$.

Note that the theory is not objective[5] in the xy plane, but it is a good approximation if the assumption $v^b \ll u^b$ holds, i.e. this simple representation is reasonable when the flow is chiefly downhill and the shearing in the xy plane is small in comparison with the shearing in the xz and yz planes. With these *ad hoc* definitions (14.37), (14.39), Koch et al. [17], Gray et al. [4] and Wieland et al. [27] obtained good agreement between theory and experiments.

The *ad hoc* definitions (14.37) and (14.39) define the earth pressure coefficients in two limiting states with piecewise constant values, respectively. There is a discontinuity at $\partial u/\partial x = 0$ or $\partial v/\partial y = 0$, which results in a jump in the in-plane pressure between convergent and divergent regions. If we consider the jump condition of the linear momentum [1], there must be a corresponding jump in the avalanche velocity, and/or the thickness, in order to balance the tractions on either side of the jump interface.

A regularization[6] for these two limiting stress states was proposed by Tai & Gray [21], in which the discontinuity is regularized by introducing a smooth transition between the two limiting stress states. This is illustrated in Fig. 14.3 for the downslope earth pressure coefficient. For large convergence they approach the passive stress state and for large divergence they approach the active stress state. Between these two limiting stress states there is a smooth monotonically decreasing transition, which crosses the $\partial u/\partial x = 0$ line at $K_x^b = K_{x_0}$ for the down slope component and $K_y^b = K_{y_0}$ at $\partial v/\partial y = 0$ for the cross slope component, where K_{x_0} and K_{y_0} are the downslope and cross slope coefficients with $\delta = \phi$, respectively. The regularized downslope and cross slope earth pressure coefficients are given by

[5] Objectivity refers here to invariance under rigid body rotations.

[6] There is no other reason for this regularization than to make the earth pressure coefficient a continuous function of the strain rate. A partial physical argument for its introduction can be found in [23].

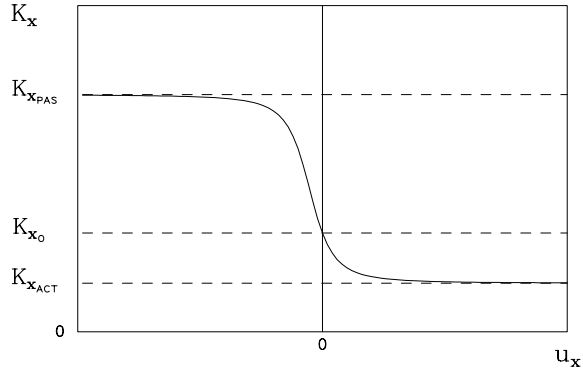

Fig. 14.3. The down slope earth pressure coefficient is regularized by introducing a smoothly varying monotonically decreasing function of the downslope divergence $\partial u/\partial x$, which approaches the limiting values, $K_{x_{\rm act}}$ and $K_{x_{\rm pass}}$, for large divergence and convergence, respectively. At $\partial u/\partial x = 0$ the downslope earth pressure coefficient equals K_{x_0}

$$
\begin{aligned}
K_x^b &= \frac{1}{2}\left\{(K_{\rm act}^x + K_{\rm pass}^x) + f_x(\partial u/\partial x)(K_{\rm act}^x - K_{\rm pass}^x)\right\} , \\
K_y^b &= \frac{1}{2}\left\{(K_{\rm act}^y + K_{\rm pass}^y) + f_y(\partial v/\partial y)(K_{\rm act}^y - K_{\rm pass}^y)\right\} ,
\end{aligned}
\tag{14.40}
$$

where the regularization functions f_x and f_y are dependent on the downslope and cross slope velocity gradients $\partial u/\partial x$ and $\partial v/\partial y$, respectively. They are chosen to be the monotonically decreasing functions

$$
\begin{aligned}
f_x(\partial u/\partial x) &= (\alpha_K \partial u/\partial x - c_0^x)/\left(1 + (\alpha_K \partial u/\partial x - c_0^x)^2\right)^{1/2} , \\
f_y(\partial v/\partial y) &= (\alpha_K \partial v/\partial y - c_0^y)/\left(1 + (\alpha_K \partial v/\partial y - c_0^y)^2\right)^{1/2} ,
\end{aligned}
\tag{14.41}
$$

where α_K determines the steepness of the transition. The constants c_0^x and c_0^y are chosen that $K_x\big|_{\partial u/\partial x=0} = K_{x_0}$ and $K_y\big|_{\partial v/\partial y=0} = K_{y_0}$, respectively[7]. Using this regularization of the earth pressure coefficients, Tai & Gray [21] demonstrated that a *necking* of the avalanche is resolved in simulating a channelized free-surface flow, in which the Wieland et al. [27] Lagrangian moving grid technique is applied. The *necking* form is observed in the transition zone when the material flows down in a channel into the horizontal flat runout zone.

14.2.6 Model Equations in Conservative Form

In the one-dimensional Savage–Hutter [19,20] theory and in the two-dimensional extensions of their theory [4,13] the downslope and cross slope pressures are

[7] The parameters K_{x_0} and K_{y_0} must be identified by experiment or via inverse methods, which is not easy. Tai et al. [23] design an experiment with rotating drums from which K_{x_0} can directly be inferred.

assumed to vary linearly over the thickness of the avalanche. In accordance with (14.32) this implies that $K_x = K_x^b$ and $K_y = K_y^b$ throughout the avalanche depth. With the traction free assumption at the free surface it follows that the average depth integrated pressures $h\langle p_{xx}\rangle$ and $h\langle p_{yy}\rangle$ [4] are determined by

$$h\langle p_{xx}\rangle = \tfrac{1}{2}h^2 K_x^b \cos\zeta + \mathcal{O}(\varepsilon^\gamma)\ , \quad h\langle p_{yy}\rangle = \tfrac{1}{2}h^2 K_y^b \cos\zeta + \mathcal{O}(\varepsilon^\gamma)\ . \tag{14.42}$$

It is also assumed that the velocity profiles are approximately uniform through the avalanche depth, i.e. all sliding and little differential shear [19]. Thus, the basal velocities are assumed to be of the form

$$u^b = \langle u\rangle + \mathcal{O}(\varepsilon^{1+\gamma})\ , \quad v^b = \langle v\rangle + \mathcal{O}(\varepsilon^{1+\gamma})\ , \tag{14.43}$$

and the velocity products can be factorised [4]

$$\begin{aligned} &\langle u^2\rangle = \langle u\rangle^2 + \mathcal{O}(\varepsilon^{1+\gamma})\ , \quad \langle uv\rangle = \langle u\rangle\,\langle v\rangle + \mathcal{O}(\varepsilon^{1+\gamma}) \\ &\text{and} \quad \langle v^2\rangle = \langle v\rangle^2 + \mathcal{O}(\varepsilon^{1+\gamma})\ . \end{aligned} \tag{14.44}$$

These assumptions are supported by measurements in large scale dry snow [2] and ping-pong ball avalanches [16].

From (14.31) and (14.44) it follows that the mass balance equation reduces to order $\varepsilon^{1+\alpha}$ to

$$\frac{\partial h}{\partial t} + \frac{\partial}{\partial x}(hu) + \frac{\partial}{\partial y}(hv) = 0\ . \tag{14.45}$$

With assumptions (14.42), (14.43) and (14.44) the depth integrated downslope (14.34) and cross slope (14.35) momentum balances yield

$$\frac{\partial}{\partial t}(hu) + \frac{\partial}{\partial x}(hu^2) + \frac{\partial}{\partial y}(huv) = hs_x - \frac{\partial}{\partial x}\left(\frac{\beta_x h^2}{2}\right)\ , \tag{14.46a}$$

$$\frac{\partial}{\partial t}(hv) + \frac{\partial}{\partial x}(huv) + \frac{\partial}{\partial y}(hv^2) = hs_y - \frac{\partial}{\partial y}\left(\frac{\beta_y h^2}{2}\right)\ , \tag{14.46b}$$

to order $\varepsilon^{1+\gamma}$, where the brackets $\langle\ \rangle$ for the mean values are dropped. The factors β_x and β_y are defined as

$$\beta_x = \varepsilon\cos\zeta K_x \quad \text{and} \quad \beta_y = \varepsilon\cos\zeta K_y\ , \tag{14.47}$$

respectively. The terms s_x and s_y represent the net driving accelerations in the downslope and cross slope directions, respectively

$$s_x = \sin\zeta - \frac{u}{|\boldsymbol{v}|}\tan\delta(\cos\zeta + \lambda\kappa u^2) - \varepsilon\cos\zeta\frac{\partial z^b}{\partial x}\ , \tag{14.48a}$$

$$s_y = \quad - \frac{v}{|\boldsymbol{v}|}\tan\delta(\cos\zeta + \lambda\kappa u^2) - \varepsilon\cos\zeta\frac{\partial z^b}{\partial y}\ , \tag{14.48b}$$

where $|\boldsymbol{v}| = (u^2+v^2)^{1/2}$. The first term at the right-hand side of (14.48a) is due to the gravitational acceleration. It has no contribution in the lateral, y, direction. The second terms of both (14.48a) and (14.48b) indicate the dry Coulomb

friction and guarantee that basal shear traction and the sliding velocity are collinear. The third terms are the contributions from the basal topography. The system of equations (14.45)–(14.46b) shall be referred to as the *two-dimensional conservative system* (2DCS) of equations.

For *smooth solutions* the mass balance can be used to simplify the convective terms in the momentum balances (14.46a), (14.46b). Providing $h \neq 0$ the mass and momentum balance equations reduce to

$$\frac{\partial h}{\partial t} + \frac{\partial}{\partial x}(hu) + \frac{\partial}{\partial y}(hv) = 0 \,, \tag{14.49a}$$

$$\frac{\partial u}{\partial t} + u\frac{\partial u}{\partial x} + v\frac{\partial u}{\partial y} = s_x - \beta_x \frac{\partial h}{\partial x} - \frac{h}{2}\frac{\partial \beta_x}{\partial x} \,, \tag{14.49b}$$

$$\frac{\partial v}{\partial t} + u\frac{\partial v}{\partial x} + v\frac{\partial v}{\partial y} = s_y - \beta_y \frac{\partial h}{\partial y} - \frac{h}{2}\frac{\partial \beta_y}{\partial y} \,, \tag{14.49c}$$

These equations and their spatially one-dimensional analogues ($\partial(\cdot)/\partial y = 0$, and (14.49c) missing) were derived earlier and numerically integrated by a Lagrangian finite difference method[8]. These cannot capture possible shocks; but they proved the model to be adequate for many avalanche tests performed in the laboratory.

14.3 Numerical Integration of the Savage–Hutter Equations

14.3.1 Standard Form of the Differential Equations and Characteristic Speeds

The two dimensional model equations (14.45)–(14.46b) can be written in general vector form

$$\frac{\partial \boldsymbol{w}}{\partial t} + \frac{\partial \boldsymbol{f}}{\partial x} + \frac{\partial \boldsymbol{g}}{\partial y} = \boldsymbol{s} \,, \tag{14.50}$$

where $\boldsymbol{w}$ denotes the vector of conservative variables, $\boldsymbol{f}$ and $\boldsymbol{g}$ represent the transport fluxes in the x- and y-directions, respectively, and $\boldsymbol{s}$ means the source

[8] The one-dimensional model was derived by Savage & Hutter [19,20] and tested against laboratory chute experiments by Greve & Hutter [5], and Hutter et al. [13]. Two-dimensional spreading was attacked by Hutter [7], Hutter et al. [13], Greve et al. [6] and Koch et al. [17] on the basis that the basal topography was flat perpendicular to the direction of steepest descent with good agreement with granular avalanches from laboratory experiments. Sidewise confinement was then incorporated in [4,27,3] with equally satisfactory agreement between model output and laboratory experiments. The chute topography in these cases was a weak parabolic channel merging into a horizontal plane.

term. They are

$$\boldsymbol{w} = \begin{pmatrix} h \\ m^x \\ m^y \end{pmatrix} , \qquad \boldsymbol{f} = \begin{pmatrix} m^x \\ (m^x)^2/h + \beta_x h^2/2 \\ m^x m^y/h \end{pmatrix} ,$$
$$\boldsymbol{g} = \begin{pmatrix} m^y \\ m^x m^y/h \\ (m^y)^2/h + \beta_y h^2/2 \end{pmatrix} , \quad \boldsymbol{s} = \begin{pmatrix} 0 \\ hs^x \\ hs^y \end{pmatrix} , \tag{14.51}$$

where the source terms in the momentum balance equations, s_x and s_y, are defined in (14.48a) and (14.48b), respectively and equations are written in the conservative variables h, $m^x = hu$ and $m^y = hv$. The spatially one-dimensional version of (14.50) is

$$\frac{\partial \boldsymbol{w}}{\partial t} + \frac{\partial \boldsymbol{f}}{\partial x} = \boldsymbol{s} , \tag{14.52}$$

where

$$\boldsymbol{w} = \begin{pmatrix} h \\ m^x \end{pmatrix} , \quad \boldsymbol{f} = \begin{pmatrix} m^x \\ (m^x)^2/h + \beta_x h^2/2 \end{pmatrix} , \quad \boldsymbol{s} = \begin{pmatrix} 0 \\ hs^x \end{pmatrix} . \tag{14.53}$$

It can be obtained from (14.51) by setting $\boldsymbol{g} = \boldsymbol{0}$ and ignoring in $\boldsymbol{w}$, $\boldsymbol{f}$ and $\boldsymbol{s}$ the third line.

The characteristic speeds of the system (14.50)–(14.51) can be computed by rewriting (14.50) as

$$\frac{\partial \boldsymbol{w}}{\partial t} + \begin{pmatrix} \boldsymbol{A}_x & 0 \\ 0 & \boldsymbol{A}_y \end{pmatrix} \begin{pmatrix} \dfrac{\partial \boldsymbol{w}}{\partial x} \\ \dfrac{\partial \boldsymbol{w}}{\partial y} \end{pmatrix} = \boldsymbol{s} , \tag{14.54}$$

where

$$\boldsymbol{A}_x := \frac{\partial \boldsymbol{f}}{\partial \boldsymbol{w}} = \begin{pmatrix} 0 & 1 & 0 \\ -(m^x)^2/h^2 + \beta_x h & 2m^x/h & 0 \\ -m^x m^y/h^2 & m^y/h & m^x/h \end{pmatrix} ,$$
$$\boldsymbol{A}_y := \frac{\partial \boldsymbol{g}}{\partial \boldsymbol{w}} = \begin{pmatrix} 0 & 0 & 1 \\ -m^x m^y/h^2 & m^y/h & m^x/h \\ -(m^y)^2/h^2 + \beta_y h & 0 & 2m^y/h \end{pmatrix} , \tag{14.55}$$

and evaluating the eigenvalues of $\boldsymbol{A}$. These follow from the characteristic equation

$$\det(\boldsymbol{A} - \lambda \boldsymbol{I}_6) = \det(\boldsymbol{A}_x - \lambda \boldsymbol{I}_3) \det(\boldsymbol{A}_y - \lambda \boldsymbol{I}_3) = 0 \tag{14.56}$$

with six solutions, given by

$$\begin{aligned} \lambda_1 &= u\ , \quad \lambda_{3,5} = m^x/h \pm \sqrt{\beta_x h}\ , \\ \lambda_2 &= v\ , \quad \lambda_{4,6} = m^y/h \pm \sqrt{\beta_y h}\ . \end{aligned} \tag{14.57}$$

The first two solutions yield as characteristic speed the particle velocity $c_p = (u^2+v^2)^{1/2}$ and as characteristic directions the streamline directions. $\lambda_{3,\ldots,6}$ give rise to four different characteristic speeds

$$\begin{aligned} C^{++} &= \left(\lambda_3^2 + \lambda_4^2\right)^{1/2}\ , \quad C^{+-} = \left(\lambda_3^2 + \lambda_6^2\right)^{1/2}\ , \\ C^{-+} &= \left(\lambda_5^2 + \lambda_4^2\right)^{1/2}\ , \quad C^{--} = \left(\lambda_5^2 + \lambda_6^2\right)^{1/2} \end{aligned} \tag{14.58}$$

with four different directions; C^{++} is the fastest and C^{--} the slowest. Whenever $c_p > C^{--}$ the flow is called *supercritical*; otherwise, i.e. when $c_p < C^{--}$, it is *subcritical*. Any transition from a supercritical to a subcritical flow state is associated with a shock. This inevitably happens when a finite avalanching mass moves down a steep slope (where it reaches supercritical speeds) and is considerably decelerated (when it approaches the runout zone) and eventually approaches a subcritical speed. This transition is always accomplished by the formation of a shock front across which the avalanche depth and speed experience sudden changes from small heights and large speeds to larger heights and smaller speeds. The numerical schemes must cope with this situation.

14.3.2 Remarks on Numerical Integration

It is not the place here to present a detailed introduction into shock-capturing numerical methods. Such an overview is given in Chap. 4 of [24]. We sketch the method only and must direct the interested reader to the literature, see [24] and [25] for detail.

Let us commence by recalling that the Lagrangian integration technique applied to the SH equations faced difficulties whenever a supercritical extending (diverging) flow became subcritical and contracting. Numerical solution in the vicinity of such transitions were accompanied with high oscillations of the depth profile and velocity field which often led to instabilities unless this was properly counteracted by a sufficient amount of numerical diffusion. The regularization of the earth pressure coefficient outlined in Sect. 14.2.5 helped to improve the situation, but the difficulties encountered with shocks were thereby not resolved.

The shock-capturing numerical methods give a high resolution of shock solutions without any spurious oscillations near a discontinuity. The traditional high order accuracy methods result in unexpected oscillations near the discontinuity. The Total Variation Diminishing (TVD) method for equation systems in conservative form achieves this goal; its application to the Savage–Hutter equations allows integration across shocks without the introduction of additional numerical diffusion.

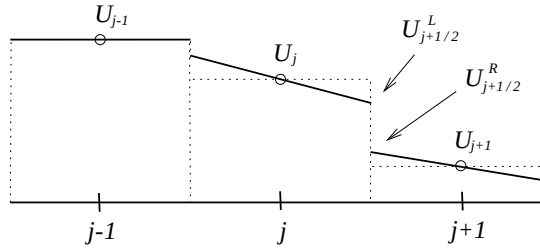

Fig. 14.4. The cell average physical value U_j (*dashed line*) and the linear piecewise cell reconstruction (*solid line*), where there are two values for each interface, e.g. $U^L_{j+1/2} = U_j + U'_j/2$ and $U^R_{j+1/2} = U_{j+1} - U'_{j+1}/2$, one from the left side cell, U_j, with the approximate derivatives U'_j, the other from the right side element, U_{j+1} with U'_{j+1}

TVD means that the sum of the variations of the variables over the whole computational domain does not increase as the time evolves. Now, the numerical schemes are designed such that they provide only the cell average values of the variable to be determined. In classical schemes of higher order approximation the numerically determined variable is continuous or even differentiable across cell boundaries. In TVD methods jump discontinuities are allowed over cell boundaries, whilst within each cell C^n-continuity may prevail, for an illustration, see Fig. 14.4.

In regions where the variations of the field variables are small no jumps are needed, but in the neighbourhood of shocks and in regions of large gradients of the field variable the cell re-constructions are such, i.e. the slopes of the variable within the cell kept so small, that possible spurious oscillations are avoided. The operators that achieve the limitation of the cell slope (just sufficient to avoid oscillations) are called *slope limiters* (and several different versions have been proposed: e.g. *Superbee, Minmod* or *Woodward*). Several schemes have been tested with the application of these three slope limiters to find the optimal scheme for smooth as well as discontinuous solutions.

There is a further numerical subtlety associated with the motion of a finite mass of granular material along an inclined plane or curved topography. The material does not occupy the whole region of topographic surface available to it but covers a region with compact support. The margin separates the regions with and without material. It can be shown that the governing equations (14.45)–(14.46b) do not admit solutions with cliffs [24] at the margin, so that margins always have vanishing avalanche height and the transition from the avalanche region to its complement is continuous. Now in an Eulerian numerical scheme with the cells fixed in space and a moving boundary problem as this one, it happens more often than not that the margin lies between the cells than exactly on cell boundaries. This is different from the Lagrangian integration technique in which the grid moves with the deforming avalanche mass and margins are always exactly traced. It is in general associated with a considerable loss of accuracy.

There are several ways out of this difficulty. One is to add a thin layer to the whole computational domain, thus abandoning the compactness of the avalanche body; a second method is to set all physical variables to zero if $h = 0$; both are not ideal and still associated with large errors close to the margin. A third method is to treat the cells in the immediate neighbourhood of the margin separately by a special *front-tracking method*. For one-dimensional flows this has been done [25], and results for the spreading of a parabolic profile turned out to be very much improved; for two-dimensional situations the method must still be developed. We now present a few computational solutions.

14.4 Examples

In this section we[9] present a number of solutions that were constructed with the shock capturing finite difference schemes developed by Tai [24]. Further results are also given in [25].

14.4.1 Similarity Solutions

For flows of a finite mass of granular materials down an inclined plane the deformation of an initially compact mass of granular materials is everywhere extending and so no shock will form in this case. The equations may then be used in the form (14.49a)–(14.49c), either in their one- or two-dimensional case. For a parabolic linear (1D) or circular (2D) initial hump at rest exact similarity solutions were constructed. These solutions ([19], 1D; [14], 1D; [11], 2D) allow determination of the asymptotic behaviour of the motion. They show that without a viscous contribution to the drag force the avalanches do not reach an asymptotic constant velocity. The parabolic profile remains preserved, but the originally circular hump becomes elliptical. Thus, the streamwise extension is larger than the cross slope extension. These exact solutions are useful, because numerical solutions obtained by other techniques can be checked against them.

It is interesting to note that such parabolic ellipses have not been observed experimentally. The profiles have rather tear drop shape [10]. These indicate that either exact initial conditions to arrive at these solutions were not realized in the experiments or the model equations – in particular the Coulomb sliding law with constant bed friction angle δ – are not adequate. The problem is still open.

14.4.2 Motion of a Granular Avalanche on an Inclined Plane Chute into the Horizontal Run-Out Zone

Shock formations are often observed when the avalanche slides from an inclined slope into the horizontal run-out zone, where the frontal part comes to rest

[9] The authors acknowledge help received from S. Noelle on shock capturing integration techniques and the software for gas dynamics from A.-K. Lie which was adopted to avalanche flow by Y.-Ch. Tai [24].

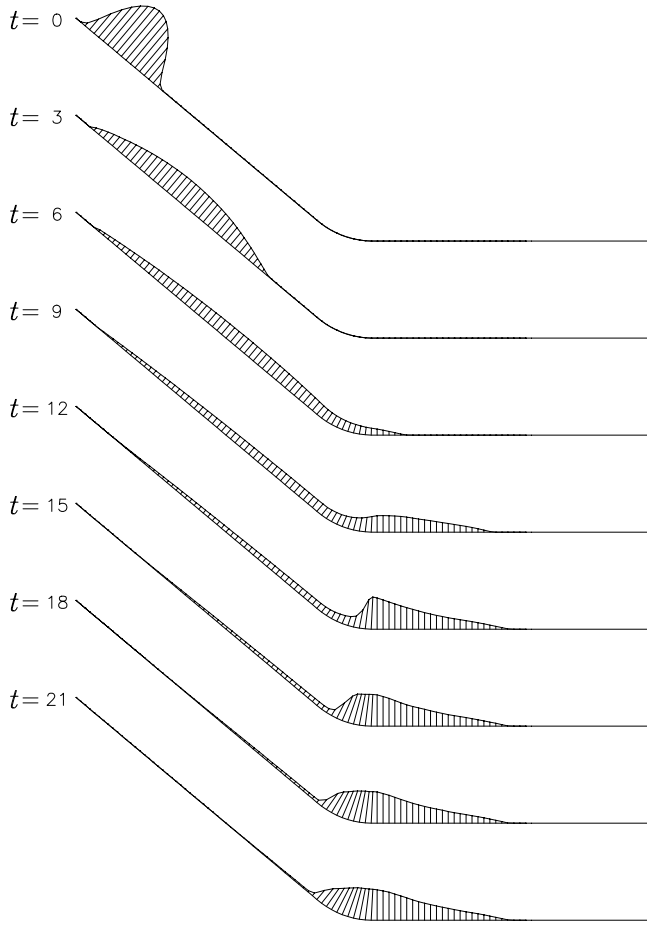

Fig. 14.5. Process of the avalanche simulated by the shock-capturing method at $t =$ 0, 3, 6, 9, 12, 15, 18, 21 dimensionless time units. As the front reaches the run-out zone and comes to rest, the rear part of the avalanche accelerates further and the avalanche body contracts. Once the velocity becomes supercritical, a shock wave develops, which moves upward.

and the part of the tail still accelerates further so that its velocity becomes supercritical. A test simulation is made by the shock-capturing method.

The granular material released from a parabolic cap slides down an inclined plane chute and merges into the horizontal run-out zone. The parabolic cap is initially located at the top of the slope with a linearly increasing velocity distribution, so that the avalanche extends by maintaining its parabolic form if it slides on an infinitely long slope [19]. The inclination angle of the inclined plane is prescribed as 40°, and a transition region lies between the inclined slope

and the run-out zone. The basal and internal friction angles are 35° and 38°, respectively.

Figure 14.5 illustrates the simulated process as the avalanche slides on the inclined plane into the horizontal run-out zone. The avalanche body extends on the inclined plane with a parabolic form ($t = 3$). Once the front reaches the horizontal run-out zone the basal friction brings the frontal part of the granular material to rest, but the part of the rear accelerates further. At this stage, if the velocity becomes super-critical, a shock (surge) wave is created ($t = 12$ to $t = 18$), which moves a short distance backwards as can clearly be seen (compare the humps at $t = 12$ to $t = 18$). At $t = 21$ the whole avalanche body comes to rest.

14.4.3 Motion of a Granular Avalanche in a Convex and Concave Curved Chute

In this section we show the simulation of a two-dimensional avalanche moving down in a confined convex and concave curved chute, and compare the result with one of many experiments, called here exp. 29 in [5]. The experiment was performed in a 10 cm wide chute of length greater than 400 cm. The basal surface was formed to follow a prescribed function, so that the inclination angle is given by

$$\zeta(x) = \zeta_0 \mathrm{e}^{-0.1x} + \zeta_1 \xi/(1+\xi^8) - \zeta_2 \exp(-0.3(x+10/3)^2) \,, \tag{14.59}$$

where

$$\xi = \tfrac{4}{15}(x-9) \,, \quad \text{and} \quad \zeta_0 = 60.0^\circ \,, \quad \zeta_0 = 31.4^\circ \,, \quad \zeta_2 = 37.0^\circ \,. \tag{14.60}$$

The influence of the confining walls of the chute on the bed friction was also considered, which was determined by replacing the bed friction angle, δ, by the *effective* bed friction angle, δ_{eff}. They are related by

$$\delta_{eff} = \delta_0 + \varepsilon k_{\mathrm{wall}} h \,; \tag{14.61}$$

here ε is the aspect ratio, h is the dimensionless depth and k_{wall} the measured correction factor to account for the side wall effects in the bed friction angle, see [12].

In the simulation all parameters are assigned as in [5], where $\delta_0 = 26.5^\circ$, $K_{\mathrm{wall}} = 11^\circ$, and the internal angle of friction is selected to be $\phi = 37^\circ$. Figure 14.6 shows the computed profile of the avalanche height on the real chute geometry. Once mobile the avalanche rapidly accelerates downslope until it reaches the shallow rise in the topography. This is enough to retard the granular material until the pressure from the material behind has sufficiently accumulated to push it over the bump. The material accelerates again and when the slope angle decreases the mass comes to rest. Normally the deposit is divided into two parts on the both sides of the bump: the rear deposit and the front deposit.

Figure 14.7 shows time slices of the computed (solid) and experimentally determined (dashed) profiles of the avalanche height for exp. 29 in [5], where $\delta_0 = 26.5^\circ$, $\phi = 37^\circ$ and $K_{\mathrm{wall}} = 11^\circ$. The division of the avalanche body into two parts is well described by the simulation.

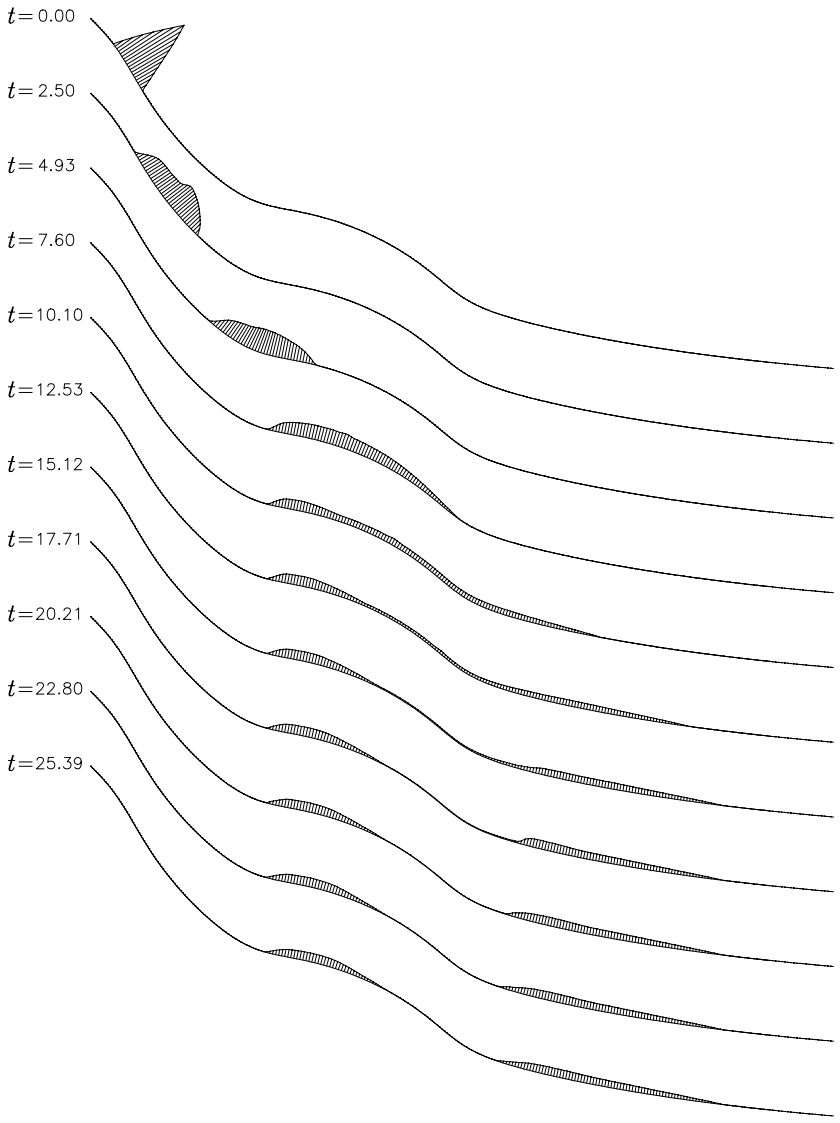

Fig. 14.6. Computed profile of the avalanche height on the real chute geometry for exp. 29 in [5]. Since compared to the length the deposited height of the avalanche is very small, the height is three times exaggerated

14.4.4 Granular Avalanche over Complex Basal Topography

In this section a simulation example on a chute with complex basal topography is presented to describe the two-dimensional shock formation. A simple reference surface is defined consisting of an inclined plane ($\zeta = 40°$) that is connected to a horizontal run-out zone ($\zeta = 0°$) by a transition zone. Superposed

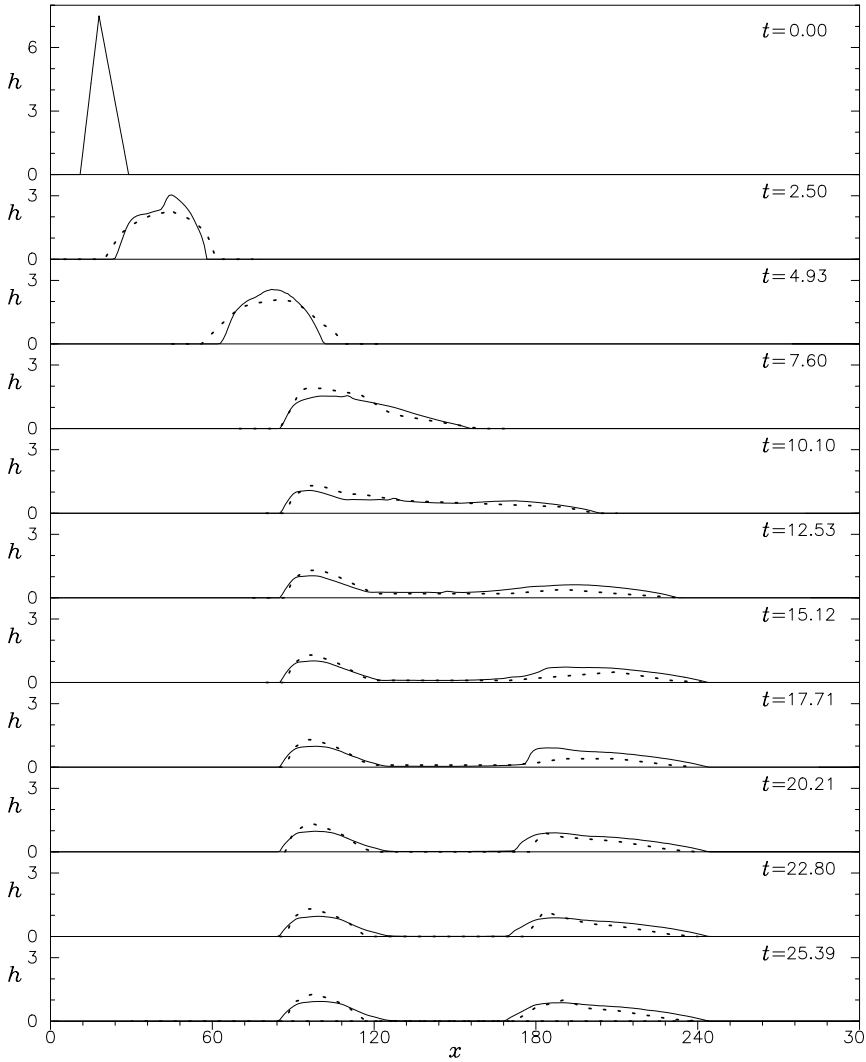

Fig. 14.7. Computed (*solid*) and experimentally determined (*dashed*) profiles of the avalanche height for exp. 29 in [5]; $\delta_0 = 26.5^\circ$, $\phi = 37^\circ$ and $K_{\text{wall}} = 11^\circ$. The horizontal distance is arc length measured along the basal surface

on the inclined section of the chute is a shallow parabolic cross-slope topography, $z^b(y) = y^2/(2R)$ with $R = 110\,\text{cm}$, which forms a channel that partly confines the avalanche motion. The inclined parabolic channel lies in the range $0 < x < 215\,\text{cm}$ and the run-out zone lies in the range $x > 245\,\text{cm}$, between which a transition zone smoothly joins the two regions. At $x = 160\,\text{cm}$ there is a small parabolic hill with radius 15 cm and heigh 5 cm, see Fig. 14.8. In the transition zone, $215 < x < 245$, a smooth change in the topography defined by

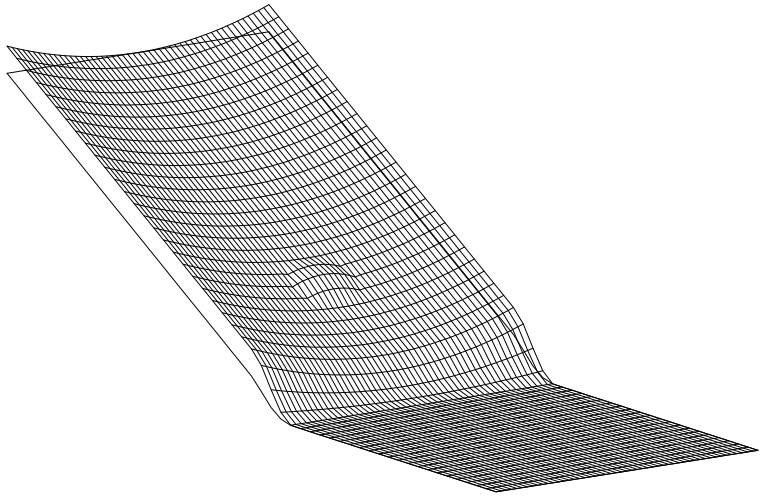

Fig. 14.8. The complex basal topography for the test problem describing the two-dimensional shock formation. A simple reference surface is defined consisting of an inclined plane that is connected to a horizontal run-out zone by a transition zone. Superposed on the reference surface is a shallow parabolic cross-slope topography, which forms a channel that partly confines the avalanche motion. The parabolic channel in restricted to the inclined range. It is connected with the horizontal run-out zone by a smooth transition zone. A small parabolic hill lies in the channel centre of the inclined portion and constitutes a partial obstruction

the inclination angle

$$\zeta(x) = \begin{cases} \zeta_0 \,, & 0 \le x \le 215 \,, \\ \zeta_0[1 - (x - 215)/40] \,, & 215 < x < 245 \,, \\ 0^\circ \,, & x \ge 245 \,, \end{cases} \tag{14.62}$$

is prescribed, where $\zeta_0 = 40^\circ$.

The simulation is performed with an internal angle of friction $\phi = 37^\circ$ and a bed friction angle $\delta = 32^\circ$. The material is suddenly released from a hemispherical shell with radius $r_0 = 32\,\text{cm}$. It is so fitted to the basal chute topography, that the projection of the line of intersection onto the reference surface is approximately elliptical in shape. The major axis of the ellipse is 32 cm long and the maximum height of the cap above the reference surface is 22 cm.

Figure 14.9 shows the depth contours of the simulated results for a sequence of non-dimensional times, from the release of the material ($t = 0$) until the

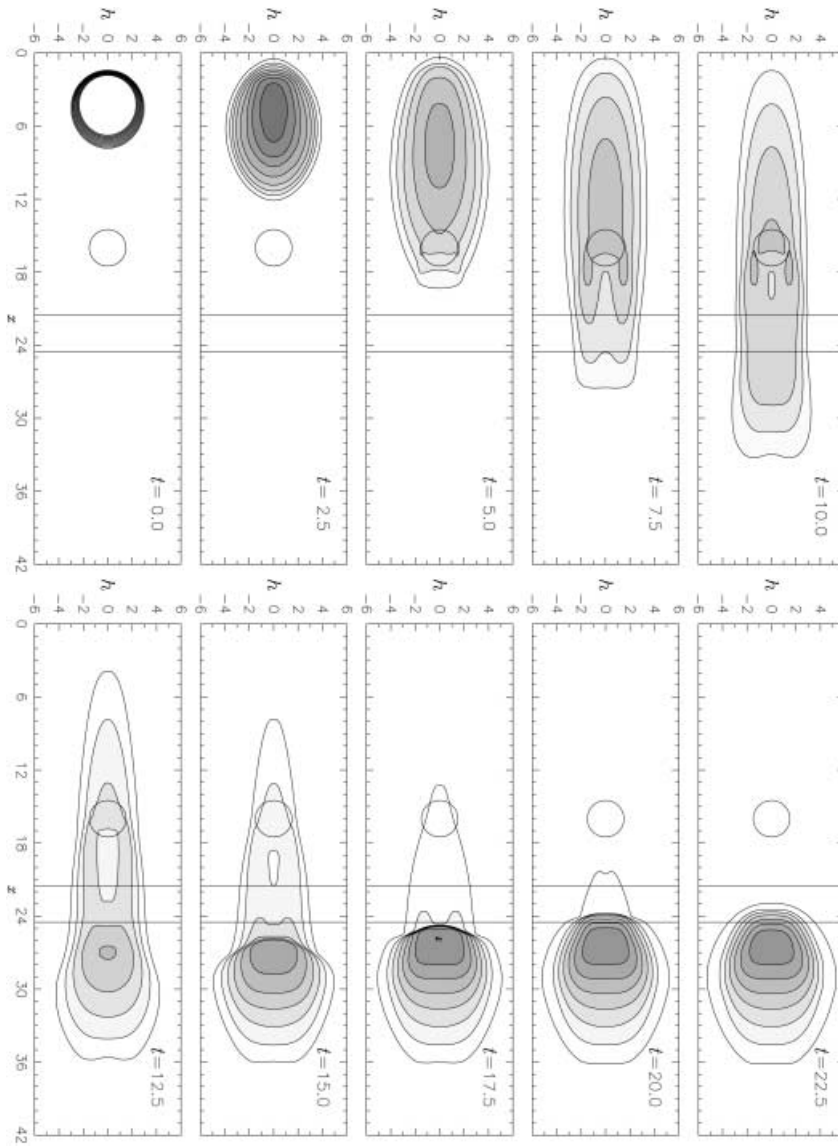

Fig. 14.9. Depth contour of the simulated results at a series of non-dimensional times, from the release of the material ($t = 0$) until the avalanche comes to rest ($t = 22.5$). The length unit is in dm

avalanche comes to rest ($t = 22.5$). Once the cap is open, the avalanche accelerates and extends, where the acceleration in the down-slope $x-$direction is obviously dominant ($t = 2.5$). Because of the back pressure the rear part of the avalanche moves slightly backwards at the initial stage of the motion. Due to

the curvature in the cross-slope direction the extension in y-direction is limited in the channel region (see $t = 5.0$ to $t = 12.5$). The hill holds the material partly up ($t = 5.0$ to $t = 12.5$), but immediately below the hill and on either side of it two knolls form. Furthermore, behind the hill the reduction of inflowing mass causes a dent to form. Basically, the material accelerates until it reaches the horizontal run-out zone. With increasing basal drag the front comes to rest ($t = 7.5$ to $t = 12.5$) but the part of the tail accelerates further. In this stage the avalanche body contracts. Once the supercritical velocity becomes subcritical, a shock wave (steep surface gradient) is formed. This occurs just after the end of the transition zone at *ca.* $x = 260$ ($t = 15$). With the approaching mass from the tail, the shock wave propagates backwards ($t = 15$ to $t = 20$), i.e., as time proceeds, this shock wave propagates upstream. At $t = 22.5$ the avalanche comes to rest.

The velocities inside the avalanche body for the same times as the avalanche geometries in Fig. 14.9 are illustrated in Fig. 14.10, in which the arrows denote the direction of the velocity, and their lengths indicate the speed. The velocity of the elements with depth $h < 0.1$ cm are not shown here. Although the hill holds the material partly up and side knolls around it and a dent behind it are formed, the velocity is not strongly affected by these features ($t = 5.0$ to $t = 12.5$) and the material is obviously accelerated in the downslope direction. The front comes to rest in the run-out zone but the part of the tail accelerates further ($t = 7.5$ to $t = 12.5$). At $t = 15$ there is obviously a jump of velocity taking place at the transition zone, which corresponds to the steep surface gradient in Fig. 14.9. With the mass approaching from the tail, the jump propagates backwards ($t = 15$ to $t = 20$). At $t = 22.5$ the avalanche comes to rest.

14.5 Concluding Remarks

In this contribution a simple theoretical model due to Savage and Hutter was presented and results obtained with it were compared with experiments. It consists of depth integrated balance laws of mass and momentum of an incompressible fluid that obeys a dry friction Coulomb type constitutive relation with constant internal angle of friction. A second phenomenological parameter entering this model is the bed friction angle which measures the roughness between the granules and the bed. This model, which is based on a shallowness assumption and supposes that downhill velocities are large in comparison to cross-channel velocities, is expressed as a hyperbolic system of partial differential equations with an (earth pressure) coefficient appearing in them which, depending on the solution, may be discontinuous. Both the hyperbolicity of the equations and the discontinuity of the earth pressure coefficient pose difficulties in the integration process and may require shock capturing numerical techniques. This requires that the differential equations are formulated in conservative form and that total variation diminishing finite difference schemes are used and combined with frontal techniques. Simulations conducted for avalanches, observed in the lab-

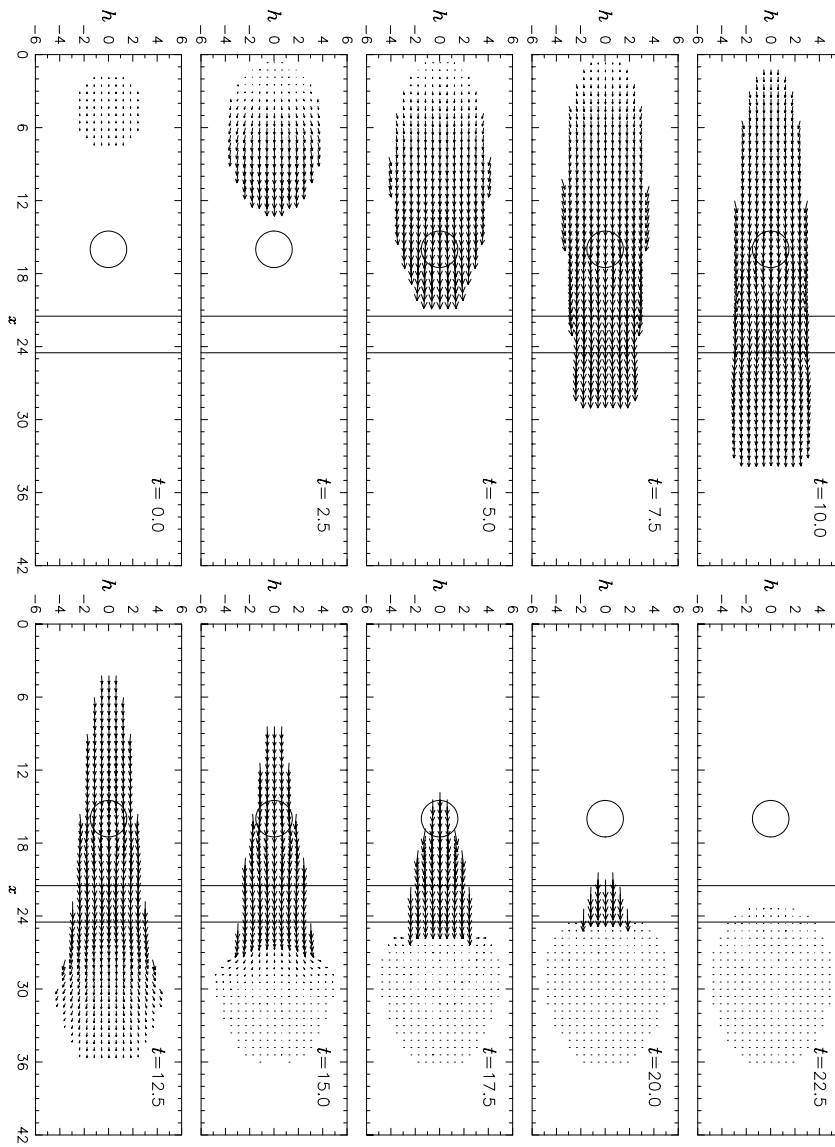

Fig. 14.10. The velocities inside the avalanche body at the same times as in Fig. 14.9 are illustrated in Fig. 14.10, in which the arrows denote the direction of the velocity and their lengths indicate the speed

oratory, show that agreement with the observations is good including in those cases when shocks are formed.

Finally we mention that the fact that the dimensionless form of the Savage–Hutter equations does not depend on any non-dimensional parameters such as

Froude, Reynolds numbers or any other π-product can constructively be used to perform laboratory experiments on rapid flow of granular materials. As a consequence, there are no scale effects in this theory, and all that must be observed in a physical model is geometric similitude and reproduction of the internal and bed friction angles. This has been done by Tai et al. [22] in a model simulation of the flow of an avalanche around a wedge that was protecting a construction. Shocks that form in such processes have also been adequately reproduced.

There remains the incorporation of entrainment/deposition processes to make the model applicable to realistic situations.

Acknowledgement

Financial support by the Deutsche Forschungsgemeinschaft through the Sonderforschungsbereich 298 is gratefully acknowledged. We thank the editors for a constructive review of the manuscript, and Y. Wang for help with the TEXing.

References

1. P. Chadwick: *Continuum Mechanics. Concise Theory and Problems* (Allen & Unwin, London 1976)
2. J.D. Dent, K.J. Burrell, D.S. Schmidt, M.Y. Louge, E.E. Adams, T.G. Jazbutis: Ann. of Glaciology, **26**, 247–252 (1998)
3. J.M.N.T. Gray, K. Hutter: Physik granularer Lawinen, Physikalische Blätter, **54** (1), 37–43 (1998)
4. J.M.N.T. Gray, M. Wieland, K. Hutter: Proc. R. Soc. London **455**, 1841–1874 (1999)
5. R. Greve, K. Hutter: Phil. Trans. R. Soc. London **A 342**, 573–604 (1993)
6. R. Greve, T. Koch, K. Hutter: Proc. R. Soc. London **A 445**, 399–413 (1994)
7. K. Hutter: Acta Mechanica (Suppl.) **1**, 167–181 (1991)
8. K. Hutter: Lawinen Dynamik – eine Übersicht. Der Maschinenschaden, **92**(5), 181–191 (1992)
9. K. Hutter: 'Avalanche Dynamics'. In: *Hydrology of Disasters*, ed. by V.P. Singh (Kluwer Academic Publ., Dordrecht–Boston–London 1996) pp. 317–394
10. K. Hutter: 'Order and disorder in granular materials'. In: *CISM, Kinetic and continuum theories of granular and porous media*, ed. by K. Hutter, K. Wilmanski (Springer, Heidelberg 1998) pp. 1–65
11. K. Hutter, R. Greve: J. Glaciology **39**, 357–372 (1993)
12. K. Hutter, T. Koch: Phil. Trans. R. Soc. London **A 334**, 93–138 (1991)
13. K. Hutter, T. Koch, C. Plüss, S.B. Savage: Acta Mechanica **109**, 127–165 (1993)
14. K. Hutter, Y. Nohguchi: Acta Mechanica **82**, 99–127 (1990)
15. K. Hutter, M. Siegel, S.B. Savage, Y. Nohguchi: Acta Mechanica **100**, 37–68 (1993)
16. S. Keller, Y. Ito, K. Nishimura: Ann. of Glaciology **26**, 259–264 (1998)
17. T. Koch, R. Greve, K. Hutter: Proc. R. Soc. London **A 445**, 415–435 (1994)
18. M.L. Lin, F.S. Jeng, C.C. Wu: Sino-Geotechnics **57**, 25–30 (1996)
19. S.B. Savage, K. Hutter: J. Fluid Mech. **199**, 177–215 (1989)
20. S.B. Savage, K. Hutter: Acta Mechanica **86**, 201–223 (1991)
21. Y.C. Tai, J.M.N.T. Gray: Annals of Glaciology, **25** 272–276 (1998)

22. Y.-C. Tai, Y. Wang, J.M.N.T. Gray, K. Hutter: 'Methods of similitude in granular avalanche flows'. In: *Advances in Cold-Region Thermal Engineering and Sciences*, ed. by K. Hutter et al. (Springer–Verlag, Berlin 1999) pp. 415–428
23. Y.-C. Tai, K. Hutter, J.M.N.T. Gray: The Chinese Journal of Mechanics **16**(2), 67–72 (2000)
24. Y.-C. Tai: Dynamics of Granular Avalanches and their Simulations with Shock-Capturing and Front-Tracking Numerical Schemes. Dissertation for Doctor Degree, Darmstadt University of Technology, Shakers Verlag, Aachen, ISBN 3-8265-7249-1, 146p (2000)
25. Y.-C. Tai, S. Noelle, J.M.N.T. Gray, K. Hutter: Shock capturing and front tracking methods for granular avalanches. J. Comput. Phys., (submitted)
26. A. Voellmy: Über die Zerstörungskraft von Lawinen, Schweizerische Bauzeitung, Jahrg. **73**, Hf 12, 159–162 (1955)
27. M. Wieland, J.M.N.T. Gray, K. Hutter: J. Fluid Mech. **392**, 73–100 (1999)